Isochoric heating of solid-density plasmas beyond keV temperature by fast thermal diffusion with relativistic picosecond laser light

Naoki Higashi [1,2,3,*] Natsumi Iwata [2,4] Takayoshi Sano [2] Kunioki Mima,[2] and Yasuhiko Sentoku [2]

[1]*Department of Physics, Graduate School of Science, Osaka University, 1-1 Machikanecho, Toyonaka, Osaka 560-0043, Japan*

[2]*Institute of Laser Engineering, Osaka University, 2-6 Yamadaoka, Suita, Osaka 565-0871, Japan*

[3]*Division of Applied Quantum Science and Engineering, Faculty of Engineering, Hokkaido University, Kita 13, Nishi 8, Kita-ku, Sapporo, Hokkaido 060-8628, Japan*

[4]*Institute for Advanced Co-Creation Studies, Osaka University, 1-1 Yamadaoka, Suita, Osaka 565-0871, Japan*

(Received 30 October 2021; accepted 31 March 2022; published 9 May 2022)

The interaction of relativistic short-pulse lasers with matter produces fast electrons with over megaampere currents, which supposedly heats a solid target isochorically and forms a hot dense plasma. In a picosecond timescale, however, thermal diffusion from hot preformed plasma turns out to be the dominant process of isochoric heating. We describe a heating process, *fast thermal diffusion*, launched from the preformed plasma heated resistively by the fast electron current. We demonstrate the fast thermal diffusion in the keV range in a solid density plasma by a series of one-dimensional particle-in-cell simulations. A theoretical model of the fast thermal diffusion is developed and we derive the diffusion speed as a function of the laser amplitude and target density. Under continuous laser irradiation, the diffusion front propagates at a constant speed in uniform plasma. Our model can provide a guideline for fast isochoric heating using future kilojoule petawatt lasers.

DOI: 10.1103/PhysRevE.105.055202

I. INTRODUCTION

The creation of high-energy-density states by isochoric heating using relativistic intensity lasers is an important issue from both fundamental and applied research perspectives. Since the invention of chirped pulse amplification (CPA) technology [1], the intensity of lasers has dramatically increased, and relativistic laser light with femtosecond to subpicosecond pulses has been actively studied for isochoric heating. Isochoric heating enables the investigation of fundamental material properties under extreme conditions such as phase transition [2], equations of states [3], opacity [4–6], thermal conductivity [7], and stopping power of high-energy particles [8]. Isochoric heating by intense lasers is also an attractive research subject, which is expected to be applied not only to the study of fundamental research, but also to a wide range of fields, such as compact high-brilliance X-rays [9], neutron sources [10], laboratory astrophysics [11], and fast ignition laser fusion [12] in inertial confinement fusion [13].

Elucidating the heat transport to overdense plasmas above the critical density has been one of the most important issues in laser isochoric heating, and the dominant process of the heat transport mechanism has changed with the development of laser devices. Since the CPA method was developed, relativistic electron beams (REBs) have been considered to play the main role in heat transport, especially in the context of fast ignition [12]. More recently, picosecond (ps) petawatt (PW) lasers, such as LFEX [14], have become accessible. Matsuo *et al.* applied the LFEX laser to heat the imploded core and achieved an electron temperature of approximately 2 keV at the core region with an energy density of 2 PPa [15]. This highly efficient heating is difficult to be explained only by REBs. The experimental and simulation results of Ref. [15] suggest that the thermal diffusion from the hot preformed plasma region, where the laser light is stopped [16] and absorbed, contributes to the core heating in addition to the REBs. The required timescale of the transition of the dominant heating mechanism from the REB to thermal diffusion is a few picoseconds [17]. In addition, thermal diffusion propagates from a hot preplasma on a picosecond timescale even after the laser pulse ends [18].

In contrast, a conventional model of isochoric heating derived by Glinsky [19] predicts that it takes a few hundred picoseconds for thermal diffusion to become dominant. There is a discrepancy of two orders of magnitude between the conventional model and the latest experiments and simulations. We construct a model to resolve this discrepancy by considering the existence of hot preplasma in front of the target and heat flow from the boundary between the preplasma and solid regions. We then clarify the parameter dependency of the "fast thermal diffusion" at keV temperature, the timescale of the transition, and the thermal diffusion speed in dense plasmas.

In this study, a series of one-dimensional (1D) particle-in-cell (PIC) simulations was performed to clarify the dependence of the fast thermal diffusion properties on both the laser and target conditions. In Sec. II, we first present the results of the parameter survey with the help of 1D PIC simulations. We then derive a theoretical model of fast thermal diffusion under picosecond PW laser irradiation in Sec. III. In the conclusion (Sec. IV), we discuss the scope of the scaling equation.

*higashi@eng.hokudai.ac.jp

II. PIC SIMULATION OF LASER ISOCHORIC HEATING

A. Simulation condition

We simulate the laser plasma interaction of kilojoule-class PW lasers. The spot radius of such a laser is as large as several tens of μm. We focus on the heat transport in the direction of the laser optical axis within this large spot radius. Therefore, the phenomena of interest can be regarded as quasi-one-dimensional, so that here we used a 1D collisional PIC code, PICLS [20].

The wavelength of the laser is 1 μm. The normalized amplitude, $a_0 = eE_L/(m_e c\omega_L)$, was varied as a_0 =1, 2, 3, 5, 7, and 11 as the simulation parameters, and for all cases the amplitude of the laser pulse rises linearly with time at a rate of $da_0/dt = 1/100$ fs, where e is the fundamental charge, E_L is the laser electric field amplitude, m_e is the electron rest mass, c is the speed of light, and ω_L is the laser angular frequency. The amplitude of the laser was kept constant after reaching the peak amplitude to simulate a 3000 $\tau_L \simeq 10$ ps interaction with a constant intensity, where τ_L is the laser period.

A 50-μm-thick, fully ionized solid density plasma was placed in a 100 μm simulation box with 20 μm of vacuum both in front of and behind the target. To include the effect of surface ablation in the interaction with the laser prepulse, a 10-μm-thick preplasma was placed in front of the target. The preplasma had an exponentially increasing density profile with a scale length of 0.32, 0.80, 1.60, or 2.56 μm, where the maximum electron density is the solid density and the minimum electron density is the critical density $n_c = \pi m_e c^2/(e^2 \lambda_L^2) = 1.11 \times 10^{21}/\lambda^2_{L,\mu m}$ cm^{-3}. The ion density of the target was set to $n_i = 25$, 50, and 100 n_c, and the atomic number of the target was set to $Z = 5$, 10, and 20.

Each cell included, e.g., 50 and 500 superparticles for ions and electrons, respectively, in the plasma region when the ion density was $n_i = 50\ n_c$ and $Z = 10$. We used a numerical resolution of $\Delta x = \lambda_L/200$ μm and $\Delta t = \tau_L/200$. At both boundaries, the outgoing electromagnetic waves were absorbed and the particles escaped from the simulation box. The Coulomb collisions between electron-electron, electron-ion, and ion-ion are included in the simulations.

B. Simulation results

Figure 1(a) shows the time evolution of the bulk electron temperature T_e inside the solid, where $x = 0$ is the location of the initial boundary position between the preplasma and solid, and $t = 0$ is the time when the peak intensity of the laser reaches the plasma surface. The energy distribution of the electrons has a hot component and a bulk component. We calculated the bulk electron temperature as the average energy of electrons with energies below 100 keV. There are two types of bulk heating components: REB heating and thermal diffusion. In the figure, REB heating is seen as a long scale tail component extending several tens of μm in the solid region, and the thermal diffusion is seen as a convex component on the top of the tail component near the solid surface. The boundary between these two components corresponds to the inflection point of the bulk electron temperature profile. The orange circles represent the diffusion front position x_f, which we define as the point of inflection of the temperature profile

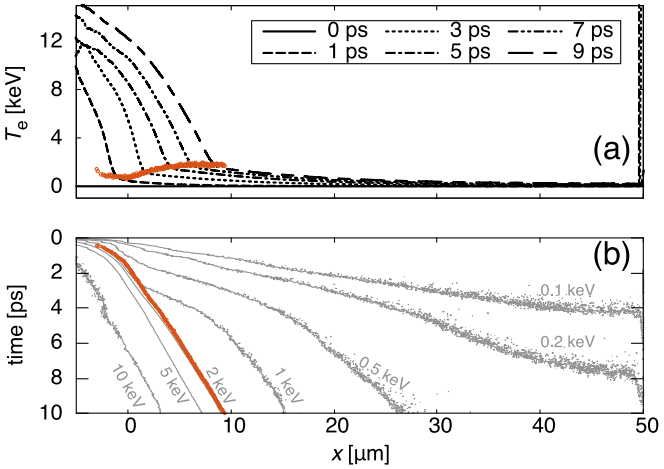

FIG. 1. (a) Temporal evolution of the bulk electron temperature in the solid target ($n_i = 50$, $Z = 10$) during the irradiation of the peak intensity ($a_0 = 1$) and trajectory of the diffusion front (orange circles). The position $x = 0$ corresponds to the initial boundary position between the preplasma and the solid. The time $t = 0$ is the time at which the laser peak reaches the position of the initial preplasma surface. (b) Time-space diagram of the bulk electron temperature T_e with contour lines. The orange circles show the trajectory of the diffusion front, as defined in (a). Each solid line is a contour line that represents $T_e = 0.1$, 0.2, 0.5, 1, 2, 5, and 10 keV.

in Fig. 1(a). Figure 1(b) shows the time-space diagram of the bulk electron temperature with the contour lines. We also show here the trajectory of the diffusion front obtained in Fig. 1(a) by orange circles. The trajectory of the diffusion front x_f can be approximated as a straight line for $x > 0$. This indicates that the thermal diffusion speed was constant over time. Next, we examine the dependence of the thermal diffusion speed on the initial parameters, especially the shape of the preplasma. In Fig. 2(b), we show the trajectories of x_f for different initial electron density profiles shown in Fig. 2(a). Here, we fix the laser normalized amplitude $a_0 = 1$, the ion density of the target $n_i = 50\, n_c$, and the atomic number of the target $Z = 10$ in all cases. As shown in Fig. 2(b), the thermal diffusion speed is constant in time for all cases, and the values of the speed for each case are almost the same. This indicates that the thermal diffusion speed does not depend on the scale length of the preplasma nor the location of the critical density from the solid surface. However, the preplasma density profile affects the arrival time of the thermal diffusion, i.e., the time at $x = 0$ in Fig. 2(b).

Although the thermal diffusion speed does not depend on the shape of the preplasma, there is a correlation between the timing of the thermal diffusion front entering the solid region $x > 0$ and the size of the preplasma. When the maximum density of the preplasma is the same, the thermal diffusion front takes more time to reach the solid surface $x = 0$ due to the critical density position being far from the surface. In the case in which the maximum density of the preplasma is different (blue), the arrival time does not show a simple dependence on the scale length. The arrival time might be determined by the amount of plasma through which the thermal diffusion front passes before reaching the solid surface. Therefore, although

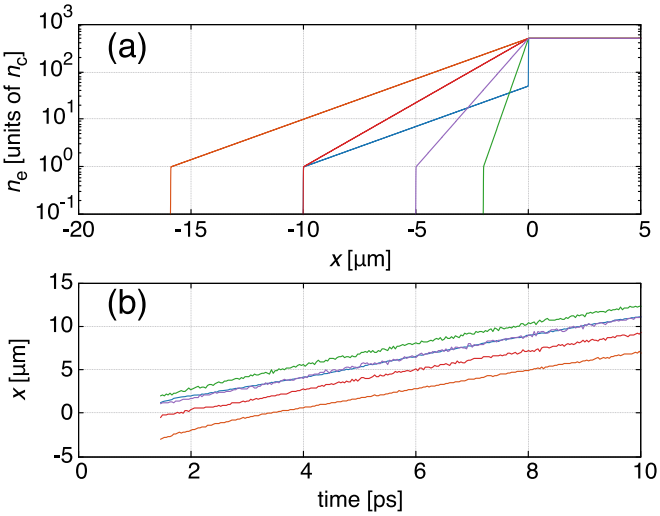

FIG. 2. (a) Initial electron density profile for each case. The scale lengths are 0.32, 0.80, 1.60, and 2.56 μm. The maximum densities of the preplasma for the cases with the scale length of 2.56 μm are 50 and 500 n_c. (b) Trajectory of thermal diffusion front in each case. The color of each line corresponds to that shown in (a).

the preplasma does not affect the thermal diffusion speed, it does affect the delivering time of thermal diffusion in the solid.

To determine the arrival time of the heat flow from the laser-plasma interface to the solid region, we show the time evolution of the electron phase plot x-p_z in Fig. 3(a) for the case in which the scale length is 2.56 μm and the maximum preplasma density is 500 n_c. Note that the present PIC simulation has a laser electric field in the y direction and plasma distributed in the x direction; thus, there is no acceleration force to induce p_z except for Coulomb collisions. The arrows in the figure indicate the inflection point of electron temperature at each observation time $t = 0.83$ ps (pink), 1.67 ps (yellow), 3.33 ps (green), and 5.0 ps (blue). The right side of the arrow was heated by Joule heating by fast electron current. The arrival time of the diffusion front at the solid interface was $t = 3.33$ ps.

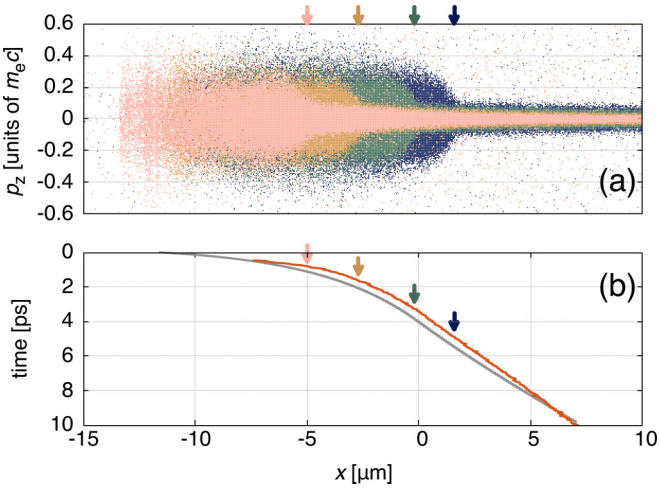

FIG. 3. (a) Temporal evolution of electron phase plot x-p_z for $a_0 = 1$, $n_i = 50$, $Z = 10$, and the preplasma scale length 2.56 μm. The arrows indicate the positions of the diffusion front at times $t =$ 0.83 ps (pink), 1.67 ps (yellow), 3.33 ps (green), and 5.0 ps (blue). (b) Trajectory of the fast thermal diffusion front in the time-space diagram. The orange line represents the result of the PIC simulation shown in (a). It is as same as the orange circles in Fig. 1(b) and the orange line in Fig. 2(b). The gray line represents the numerical solution of Eq. (2) with the factor $f = 0.1$. The arrows indicate the observation times in (a).

III. THEORETICAL MODELING OF FAST THERMAL DIFFUSION

In this section, we develop a theoretical model by considering the situation observed in the PIC simulations described in the previous section. According to the conventional model [19], the time required for thermal diffusion to be dominant compared with the REB heating is approximately a few hundred picoseconds, which is approximately two orders of magnitude longer than what we observed in the PIC simulations. Here we derive a scaling equation for fast thermal diffusion occurring on a few picoseconds by taking into account a preplasma that was not considered in the conventional model.

Through the interaction with the main pulse, the overcritical density preplasma is heated beyond keV temperature by Joule heating, and the hot region proceeds diffusively to the solid interface, as shown in Fig. 3(a). It is thus important to consider the dynamics of the preplasma heating to determine the boundary condition of the solid interface, which was not considered in the conventional model. Because of the heat flow from the hot interface, our model predicts a much shorter time than the conventional model to drive the fast thermal diffusion from the solid surface.

The time evolution of the bulk electron temperature can be described as follows [19]:

$$\frac{3}{2}\bar{n}_e\frac{\partial \bar{T}_e}{\partial \bar{t}} = \bar{\eta}\bar{j}_h^2 + \frac{3}{2}\frac{\bar{n}_h\bar{T}_h}{\bar{\tau}_{eh}(\bar{T}_h)} + \frac{\partial}{\partial \bar{x}}\left[\bar{\kappa}(\bar{T}_e)\frac{\partial \bar{T}_e}{\partial \bar{x}}\right], \qquad (1)$$

where $\bar{n}_e$ and $\bar{n}_h$ are the bulk electron density and the hot electron density normalized by the critical density n_c, and $\bar{T}_e$ and $\bar{T}_h$ are the bulk electron temperature and the hot electron temperature normalized by the electron mass energy $m_e c^2$, respectively. $\bar{t}$ is the time normalized by the laser oscillation period τ_L. $\bar{\eta} = \bar{\eta}_0 Z \ln\Lambda/\bar{T}_e^{3/2}$ with the Coulomb logarithms $\ln\Lambda$, and a constant $\bar{\eta}_0 = e^2\omega_L/(m_e c^3) \approx 1.6\times10^{-8}$. $\bar{j}_h = \bar{n}_h\,\bar{v}_h$, where $\bar{v}_h$ is the hot electron flow velocity normalized by the speed of light c, and the current density is normalized by $en_c c$. $\bar{\tau}_{eh}$ is the collision time between the bulk electrons and hot electrons. $\bar{\kappa}(\bar{T}_e) = \alpha_{SH}\, f\,(\lambda_L^3\, n_c/\pi^2)\bar{T}_e^{5/2}/(\ln\Lambda\, Z)$ is the thermal conductivity of electrons, where $\alpha_{SH} = 16\sqrt{2}/\pi^{3/2}$ is the coefficient of Spitzer-Härm thermal conductivity [21,22], and f (<1) is a factor that expresses the effect of suppressing the heat flux. This factor should be considered when there is a steep temperature gradient that can be found in laser plasmas. In this simulation, the ratio λ_{ei}/L_T is approximately 1/20, where λ_{ei} is the collision mean free path between ions and electrons for an electron with 10 keV in the solid density and L_T is the scale length of the electron temperature gradient. The

terms on the right-hand side of Eq. (1) correspond to Joule heating, drag heating, and thermal diffusion, respectively.

We solve Eq. (1) numerically by omitting the Joule heating and the drag heating terms to only observe the dynamics of the fast thermal diffusion front. Here, we assume that the laser and plasma density distributions are the same as those in the PIC simulation shown in Fig. 3(a). To solve the equation, the temporal evolution of the electron temperature at the relativistic critical density by Joule heating [23] is used as the boundary condition with an absorption rate of 10%, which was observed in the PIC simulation. In Fig. 3(b), a gray line represents the trajectory of the fast thermal diffusion front obtained from the numerical solution of Eq. (2). We also show the fast thermal diffusion front in the PIC simulation using an orange line. The good agreement between the results of the PIC simulation and the numerical solution indicates that fast thermal diffusion propagates through the preplasma and solid regions. Because the thermal spread in the phase space in the preplasma was almost uniform behind the diffusion front, as shown in Fig. 3(a), the temperature at the critical density, i.e., at the laser-plasma interface, can be used as the boundary condition at the solid surface after the heat front reaches the solid surface.

To derive the analytical formula of the fast thermal diffusion speed, we consider only the thermal diffusion term in the energy equation as

$$\frac{\partial \bar{T}_e}{\partial \bar{t}} = \frac{\partial}{\partial \bar{x}}\left(-a\bar{T}_e^{\frac{5}{2}}\frac{\partial \bar{T}_e}{\partial \bar{x}}\right), \tag{2}$$

where $a \equiv 2\bar{n}_e\,\bar{\kappa}(\bar{T}_e)\bar{T}_e^{-5/2}/3$. We then assume a convex temperature profile of $\bar{T}_e$ in the solid region to satisfy Eq. (2) as $\bar{T}_e(\bar{x},\,\bar{t}) = A(\bar{v}_{heat}\,\bar{t} - \bar{x})^{2/5}$ [24–26], where $\bar{v}_{heat}$ is the speed of the propagation front of the fast thermal diffusion, and $\bar{v}_{heat}\bar{t}\,(>\bar{x})$ indicates the location of the diffusion front at time $\bar{t}$. Here, the coefficient A is $A = [(5/2)\bar{v}_{heat}/a]^{2/5}$.

The boundary of the solid surface is located at $x = 0$. In the region $x < 0$, the preplasma is heated by the Joule heating as

$$\frac{3}{2}\bar{n}_p\frac{\partial\,\bar{T}_p}{\partial\,\bar{t}} = \frac{\bar{\eta}_0\,Z\,\ln\Lambda\,(\bar{n}_h\,\bar{v}_h)^2}{\bar{T}_p^{\frac{3}{2}}}, \tag{3}$$

where $\bar{T}_p$ and $\bar{n}_p$ are the normalized preplasma electron temperature and density, respectively. Here, we neglect the drag heating which is not efficient at the solid density in the current spatial scale. We also neglect the plasma wave heating [27] and fast ion heating to obtain a simple scaling. Such kinetic effects will be important for interactions at higher laser intensities. By solving Eq. (3), we obtain $T_p(t)$ with the initial condition $T_p(0) = 0$ as

$$\bar{T}_p(\bar{t}) = \left[\frac{5\,\bar{\eta}_0\,\ln\Lambda\,Z\,(\bar{n}_h\,\bar{v}_h)^2\,\bar{t}}{3\,\bar{n}_p}\right]^{2/5}. \tag{4}$$

The boundary condition at $x = 0$ for Eq. (2) is then given by $\bar{T}_e(0,\bar{t}) = \bar{T}_p(\bar{t})$. Hereafter, we replace n_p in Eq. (4) by n_h, considering that the spread of p_z in the preplasma region was almost uniform in Fig. 3(a). Using this boundary condition,

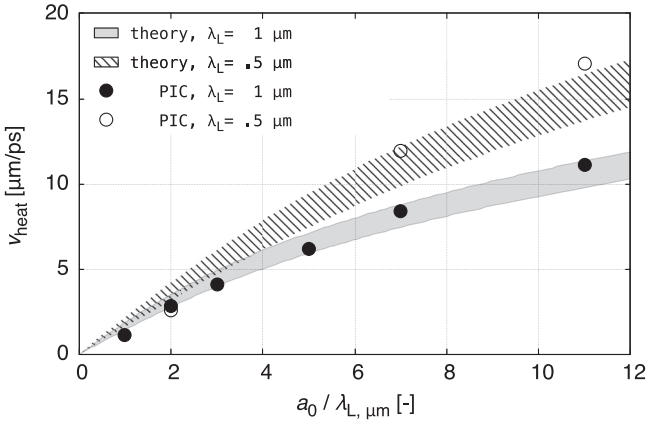

FIG. 4. Fast thermal diffusion speed v_{heat} vs $a_0/\lambda_{L,\,\mu m}$ ($\propto I^{1/2}$). The target parameters were fixed ($n_i = 50$, $Z = 10$). Black dots and white circles represent the simulation results for $\lambda_L = 1.0$ and 0.5 μm, respectively. The gray shaded area and striped area are v_{heat} obtained from Eq. (5) with the factor $f = 0.065$ and the absorption rate $\chi_{ab} = 0.1$–0.17 for $\lambda_L = 1.0$ μm and $\chi_{ab} = 0.13$–0.22 for $\lambda_L = 0.5$ μm, respectively.

we get the fast thermal diffusion speed from Eq. (2) as

$$\begin{aligned}\bar{v}_{heat} &= \left(\frac{8}{9}\,\alpha_{SH}\,f\right)^{\frac{1}{2}}\left(\frac{n_h}{n_e}\right)^{\frac{1}{2}}\bar{v}_h \\ &= \frac{1.9\,f}{\sqrt{\bar{n}_i\,Z}}\sqrt{\frac{\gamma^2-1}{\gamma}}.\end{aligned} \tag{5}$$

The second equation is derived using the relations $n_h = \gamma\,n_c$, $n_e = n_i\,Z$, $\bar{v}_h = \sqrt{(\gamma^2-1)}/\gamma$. We determine the value of factor f by fitting the analytical function of Eq. (5) to PIC simulation results. Here, the Lorenz factor of hot electrons is $\gamma \equiv \sqrt{1 + \chi_{ab}a_0^2/2}$ [23] with the laser energy absorption rate χ_{ab}.

As shown in the right-hand side of Eq. (5), the fast thermal diffusion speed is expressed by the square root of the density ratio of hot electrons to bulk electrons multiplied by the hot electron velocity. Note that $\bar{v}_{heat}$ is constant in time. The constant velocity is attributed to the temporal evolution of the electron temperature in the preplasma heated by Joule heating. We also see that $\bar{v}_{heat}$ has control parameters, i.e., laser normalized amplitude a_0 in γ, and target electron density $n_iZ = n_e$.

Figure 4 shows the dependence of fast thermal diffusion speed on $a_0/\lambda_{L,\,\mu m}$ which is proportional to the square root of laser intensity I. The simulations were performed with varying the laser normalization amplitude a_0 while the target ion density was fixed at $n_i = 50$ and the atomic number at $Z = 10$. The simulation results are shown as black dots for $\lambda_{L,\,\mu m} = 1.0$, and white circles for $\lambda_{L,\,\mu m} = 0.5$. The theoretical scaling given by Eq. (5) for $\lambda_{L,\,\mu m} = 1.0$ with the absorption rate of 10–17%, which is determined by the simulation result, is shown by the gray shaded area. The factor f in Eq. (5) is determined by fitting Eq. (5) for all black dots in Fig. 4 assuming that the absorption rate is 13.5%, which is the mean value of the simulation results. As a result of the fitting, the factor is $f \approx 0.065$. As shown in the figure, the theoretical

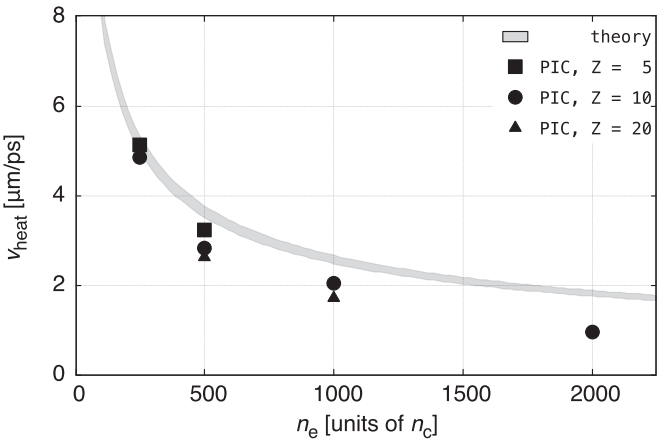

FIG. 5. Fast thermal diffusion speed v_{heat} vs target electron density n_e when the laser normalized amplitude and the laser wavelength are fixed ($a_0 = 2$ and $\lambda_L = 1.0$). The black square, circle, and triangle dots represent the simulation results of $Z = 5$, 10, and 20, respectively. The gray shaded area is the result of the theoretical model with the absorption rate $\chi_{ab} = 0.17$–0.2.

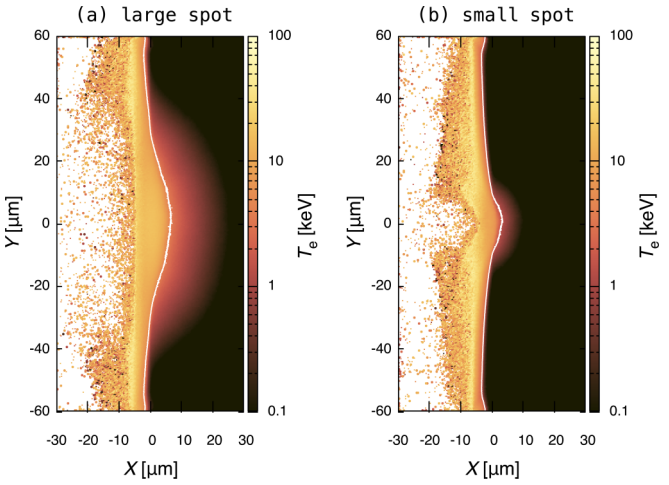

FIG. 6. 2D heat map of electron temperature at $t = 1000\,\tau$ for $\phi_L \approx 50\ \mu$m (large), and $\phi_L \approx 7\ \mu$m (small). The white line is the contour of electron temperature of the inflection point at the center, $Y = 0$. The parameters for the two-dimensional simulation are as follows: A 1.65 ps (500 τ_L) flat-top laser pulse ($\lambda_L = 1\ \mu$m) is injected from the left boundary with the peak intensity of $a_0 = 1.4$. The pulse has a Gaussian rising edge with the time width of 2.31 ps (700 τ_L). The laser focused spot size (FWHM) was set to $\phi_L \approx 50\ \mu$m (large) and 7 μm (small). The laser was irradiated perpendicular to the target surface. A 30-μm-thick aluminum with the ion density of 59.8 n_c (2.7 g/cc) is placed in a $60 \times 120\ \mu$m simulation box with 20 μm of vacuum in front of the target. Note here that we start from the partially ionized aluminum ($Z = 1$). Each cell includes 2 and 26 superparticles for ions and electrons, respectively, in the plasma region. We used a numerical resolution of $\Delta x = \Delta y = 1/50\ \mu$m and $\Delta t = \tau_L/50$, where τ_L is the laser period.

prediction of the dependence on the intensity is consistent with the simulation results over the range of approximately one order of magnitude. This range corresponds to 10^{18} to 10^{20} W/cm^2, which covers the current spec of kilojoule PW lasers.

The fast thermal diffusion speed v_{heat}, given by Eq. (5), is higher for the shorter laser wavelength because n_h is proportional to n_c, which is higher for shorter laser wavelength. For instance, when we decrease the laser wavelength by half, v_{heat} becomes approximately $\sqrt{2}$ times faster for $a_0 \gg 1$. The striped area in Fig. 4 represents Eq. (5) with $\lambda_{L,\,\mu m} = 0.5$ and the absorption rate 13–22% observed in the simulations. The theoretical model predicts that the difference in v_{heat} is larger for higher intensities. The PIC simulation results agree well with this trend of the prediction. The result indicates that for the same laser intensity, a laser with a shorter wavelength is beneficial for fast thermal diffusion.

Figure 5 shows the dependence of the fast thermal diffusion speed on the electron density of the target. The laser normalized amplitude is fixed at $a_0 = 2$, and the electron density of the target is simulated with different combinations of ion density and atomic numbers. The results of the simulation are shown as black dots. The square, circle, and triangular dots represent the results for $Z = 5$, 10, and 20, respectively. The gray dotted line is the theoretical scaling equation with a value of 10% absorption substituted. The theoretical model also explains the simulation results well for the electron density dependence of the target. In terms of mass density, the validation was performed in the range of 0.9 to 7.5 g/cm^3. This is sufficient to cover the range of general solid density plasmas.

The theoretical model derived above is based on simple assumptions, but it can explain the fast thermal diffusion speed in solid density plasmas by kilojoule PW lasers.

We performed two-dimensional (2D) collisional PIC simulations to investigate the multidimensional effect of fast thermal diffusion. The heat map of the electron temperature $t = 3.3$ ps, which is 0.8 ps after the laser irradiation with the peak intensity starts, is shown in Fig. 6. Substituting the parameters ($n_i = 59.8, Z = 13, f = 0.1, \chi_{ab} = 0.4, a_0 = 1.4$) used in the 2D calculation into Eq. (5), the thermal diffusion speed becomes 3.7 μm/ps. The thermal diffusion speed v_{heat} in the 2D simulation with a large spot (spot diameter $\phi_L = 50\ \mu$m) is 3.8 μm/ps, which is consistent with Eq. (5). In a small spot simulation ($\phi_L = 7\ \mu$m), v_{heat} decreases to 2.8 μm/ps by the multidimensional effect. Note that the thermal diffusion speed in the 2D simulation is calculated from the speed of the inflection point of the temperature gradient at $Y = 0$. We confirmed that Eq. (5) could be applied when the spot size is large, so that the one dimensionality of the system is maintained.

IV. CONCLUSION AND DISCUSSION

In this study, we demonstrate the keV range fast thermal diffusion in the interaction between solid density plasmas and a kilojoule PW laser light using a series of 1D collisional PIC simulations. We also conducted a parameter survey to clarify the heating mechanism of the fast thermal diffusion. When laser heating maintains the preplasma at high temperatures on the timescale of picoseconds, a keV temperature heat wave is launched from the preplasma region and propagates through the solid density plasma. It was shown that the fast thermal diffusion speed is constant over time in the

solid region. We derived the fast thermal diffusion speed by considering the presence of the preplasma. The model shows that fast thermal diffusion starts much earlier than that in the conventional model. This is because the fast thermal diffusion is driven by the hot electrons with energies of a few tens keV of which the mean free path is about two orders of magnitude less than that of sub-MeV fast electrons considered in the conventional model. The time needed to launch the keV range fast thermal diffusion into the solid region depends on the preplasma volume. The fast thermal diffusion could be more effective with shorter laser wavelength if the intensity is the same.

We estimate the effect of radiation loss in the keV range isochoric heating. For simplicity, we consider temperature evolution by bremsstrahlung radiation loss [28] as $d\,\bar{T}_e/d\,\bar{t} = -5.48 \times 10^{-10}\,\bar{n}_i\,Z^2\,\bar{T}_e^{\frac{1}{2}}$. By solving this equation, the time $\bar{t}_{cool}$ for the initial temperature $\bar{T}_{ini}$ can be expressed as $\bar{t}_{cool} = \bar{T}_{ini}/(5.48 \times 10^{-10}\,\bar{n}_i\,Z^2)$. For instance, in the case of fully ionized aluminum, $Z = 13$, $\bar{n}_i = 53.6$, and $T_{ini} = 10$ keV, the cooling time is $t_{cool} \approx 13$ ps. In other words, the effect of radiation loss of aluminum plasmas is considered to be small for the pulse duration of current kilojoule PW lasers, which is typically less than 10 ps. Similarly, considering fully ionized silver ($Z = 47$), the cooling time of 10 keV is $t_{cool} \approx 1.0$ ps, and the effect of radiation loss is not negligible. When Z is approximately 15 or more, the cooling time at solid density ($\bar{n}_i = 50$) for $T_{ini} = 10$ keV is less than 10 ps. In the isochoric heating of 10-keV-temperature solid density plasmas by the current kilojoule PW laser, we can roughly estimate that the effect of radiation loss can be neglected for materials with $Z \leqslant 15$.

Our model is limited to the 1D geometry, that is, the model is applicable until the heated depth is less than the laser spot radius. The fast thermal diffusion speed slows down after the diffusion front propagates over a distance comparable to the spot radius. The self-generated magnetic field and the external magnetic field applied in the direction of the laser optical axis might help to sustain the quasi-one-dimensionality by suppressing the thermal diffusion in the lateral direction. Future work should investigate fast thermal diffusion in multidimensional situations in detail.

ACKNOWLEDGMENTS

N.H. was partially supported by a Grant-in-Aid for JSPS Fellow Grant No. 20J10511 and the Iue Memorial Foundation. This study was supported by JSPS KAKENHI Grants No. JP19KK0072, No. JP20K14439, No. JP20H00140, and by JST, PRESTO Grant No. JPMJPR21O1.

[1] D. Strickland and G. Mourou, Compression of amplified chirped optical pulses, Opt. Commun. **55**, 447 (1985).

[2] Y. Sentoku, I. Paraschiv, R. Royle, R. C. Mancini, and T. Johzaki, Kinetic effects and nonlinear heating in intense x-ray-laser-produced carbon plasmas, Phys. Rev. E **90**, 051102(R) (2014).

[3] G. M. Dyer, A. C. Bernstein, B. I. Cho, J. Osterholz, W. Grigsby, A. Dalton, R. Shepherd, Y. Ping, H. Chen, K. Widmann, and T. Ditmire, Equation-of-State Measurement of Dense Plasmas Heated With Fast Protons, Phys. Rev. Lett. **101**, 015002 (2008).

[4] P. Audebert, R. Shepherd, K. B. Fournier, O. Peyrusse, D. Price, R. Lee, P. Springer, J.-C. Gauthier, and L. Klein, Heating of Thin Foils with a Relativistic-Intensity Short-Pulse Laser, Phys. Rev. Lett. **89**, 265001 (2002).

[5] P. Audebert, P. Renaudin, S. Bastiani-Ceccotti, J.-P. Geindre, C. Chenais-Popovics, S. Tzortzakis, V. Nagels-Silvert, R. Shepherd, I. Matsushima, S. Gary, F. Girard, O. Peyrusse, and J.-C. Gauthier, Picosecond Time-Resolved X-Ray Absorption Spectroscopy of Ultrafast Aluminum Plasmas, Phys. Rev. Lett. **94**, 025004 (2005).

[6] S. N. Chen, G. Gregori, P. K. Patel, H.-K. Chung, R. G. Evans, R. R. Freeman, E. Garcia Saiz, S. H. Glenzer, S. B. Hansen, F. Y. Khattak, J. A. King, A. J. Mackinnon, M. M. Notley, J. R. Pasley, D. Riley, R. B. Stephens, R. L. Weber, S. C. Wilks, and F. N. Beg, Creation of hot dense matter in short-pulse laser-plasma interaction with tamped titanium foils, Phys. Plasmas **14**, 102701 (2007).

[7] A. McKelvey, G. Kemp, P. Sterne, A. Fernandez-Panella, R. Shepherd, M. Marinak, A. Link, G. Collins, H. Sio, J. King *et al.*, Thermal conductivity measurements of proton-heated warm dense aluminum, Sci. Rep. **7**, 7015 (2017).

[8] J. A. Frenje, P. E. Grabowski, C. K. Li, F. H. Séguin, A. B. Zylstra, M. Gatu Johnson, R. D. Petrasso, V. Y. Glebov, and T. C. Sangster, Measurements of Ion Stopping Around the Bragg Peak in High-Energy-Density Plasmas, Phys. Rev. Lett. **115**, 205001 (2015).

[9] J. Workman, M. Nantel, A. Maksimchuk, and D. Umstadter, Application of a Picosecond Soft x-ray Source to Time-Resolved Plasma Dynamics, Appl. Phys. Lett. **70**, 312 (1997).

[10] O. Komeda, Y. Nishimura, Y. Mori, R. Hanayama, K. Ishii, S. Nakayama, Y. Kitagawa, T. Sekine, N. Sato, T. Kurita *et al.*, First demonstration of laser engagement of 1-Hz-injected flying pellets and neutron generation, Sci. Rep. **3**, 2561 (2013).

[11] S. V. Bulanov, T. Z. Esirkepov, D. Habs, F. Pegoraro, and T. Tajima, Relativistic laser-matter interaction and relativistic laboratory astrophysics, Eur. Phys. J. D **55**, 483 (2009).

[12] M. Tabak, J. Hammer, M. E. Glinsky, W. L. Kruer, S. C. Wilks, J. Woodworth, E. M. Campbell, M. D. Perry, and R. J. Mason, Ignition and high gain with ultrapowerful lasers*, Phys. Plasmas **1**, 1626 (1994).

[13] J. Nuckolls, L. Wood, A. Thiessen, and G. Zimmerman, Laser compression of matter to super-high densities: Thermonuclear (CTR) applications, Nature (London) **239**, 139 (1972).

[14] N. Miyanaga, H. Azechi, K.A. Tanaka, T. Kanabe, T. Jitsuno, J. Kawanaka, Y. Fujimoto, R. Kodama, H. Shiraga, K. Knodo, K. Tsubakimoto, H. Habara, J.Lu, G. Xu, N. Morio, S. Matsuo, E. Miyaji, Y. Kawakami, Y. Izawa, and K. Mima, 10-kj pw laser for the FIREX-I program, J. Phys. IV France **133**, 81 (2006).

[15] K. Matsuo, N. Higashi, N. Iwata, S. Sakata, S. Lee, T. Johzaki, H. Sawada, Y. Iwasa, K. F. F. Law, H. Morita, Y. Ochiai, S. Kojima, Y. Abe, M. Hata, T. Sano, H. Nagatomo, A. Sunahara, A. Morace, A. Yogo, M. Nakai *et al.*, Petapascal Pressure

Driven by Fast Isochoric Heating with a Multipicosecond intense Laser Pulse, Phys. Rev. Lett. **124**, 035001 (2020).

[16] N. Iwata, S. Kojima, Y. Sentoku, M. Hata, and K. Mima, Plasma density limits for hole boring by intense laser pulses, Nat. Commun. **9**, 623 (2018).

[17] N. Higashi, N. Iwata, T. Sano, K. Mima, and Y. Sentoku, Transition of dominant heating process from relativistic electron beam heating to thermal diffusion in an over picoseconds relativistic laser-solid interaction, High Energy Density Phys. **37**, 100829 (2020).

[18] H. Sawada, Y. Sentoku, T. Yabuuchi, U. Zastrau, E. Förster, F. N. Beg, H. Chen, A. J. Kemp, H. S. McLean, P. K. Patel, and Y. Ping, Monochromatic 2D K α Emission Images Revealing Short-Pulse Laser Isochoric Heating Mechanism, Phys. Rev. Lett. **122**, 155002 (2019).

[19] M. E. Glinsky, Regimes of suprathermal electron transport, Phys. Plasmas **2**, 2796 (1995).

[20] Y. Sentoku and A. J. Kemp, Numerical methods for particle simulations at extreme densities and temperatures: Weighted particles, relativistic collisions and reduced currents, J. Comput. Phys. **227**, 6846 (2008).

[21] L. Spitzer, *Physics of Fully Ionized Gases* (Interscience Publishers, New York, 1962).

[22] P. Gibbon, *Short Pulse Laser Interactions with Matter* (Imperial College Press, London, 2005).

[23] P. Leblanc and Y. Sentoku, Scaling of resistive guiding of laser-driven fast-electron currents in solid targets, Phys. Rev. E **89**, 023109 (2014).

[24] Y. B. Zel'dovich and Y. P. Raizer, *Physics of Shock Waves and High-temperature Hydrodynamic Phenomena*, Vol. 2 (Academic Press, Cambridge, MA, 1968).

[25] F. J. Mayer, J. F. McGrath, and J. W. Steele, A class of similarity solutions for the nonlinear thermal conduction problem, J. Phys. A: Math. Gen. **16**, 3393 (1983).

[26] P. Mulser, *Hot Matter from High-Power Lasers* (Springer, Berlin, 2020).

[27] M. Sherlock, E. G. Hill, R. G. Evans, S. J. Rose, and W. Rozmus, In-Depth Plasma-Wave Heating of Dense Plasma Irradiated by Short Laser Pulses, Phys. Rev. Lett. **113**, 255001 (2014).

[28] A. S. Richardson, *2019 NRL Plasma Formulary* (Naval Research Laboratory, Washington, DC, 2019).